The importance of flow history in mixed shear and extensional flows

Caroline E. Wagner, Gareth H. McKinley*

Hatsopoulos Microfluidics Laboratory, Department of Mechanical Engineering, Massachusetts Institute of Technology, Cambridge, MA 02139, United States

ARTICLE INFO

ABSTRACT

Many complex fluid flows of industrial and academic interest exhibit mixed kinematics with localized regions of shear and elongation. Examples include converging flows (e.g. through planar hyperbolic contractions in microfluidic devices), flows through porous media, and polymer processing flows past submerged obstacles (e.g. 'spiders' and mandrels). For polymer solutions, characterization of 2D flow as locally shear or extensional in character is particularly important for analysis, as these 'weak' and 'strong' flows, respectively, orient and deform polymer chains in very different ways. Through the introduction of a 'flow-type parameter' α which varies between 0 in simple shear to 1 in planar elongation, the local velocity fields of all such mixed two-dimensional flows can be concisely characterized. We determine an analytic expression for the stress field of an Oldroyd-B fluid for two different flow histories: (i) constant strain rate and constant (but arbitrary $0 \leq \alpha \leq 1$) flow-type parameter, and (ii) constant strain rate and time varying flow-type parameter ($0 \leq \alpha(t) \leq 1$). We demonstrate that both the flow strength and kinematic sequencing (i.e. whether the flow is initialized in shear or elongation) are critical for determining the local dynamical response of material elements as a result of the fluid's fading memory of the entire deformation history, and can only be ignored in the limit of infinitely slow variations. Finally, we consider the flow of an Oldroyd-B fluid around a circular cylinder, and show that by treating the instantaneous polar angle $\theta(t)$ as the flow type parameter, the elastic and viscous contributions to the stress field can be analyzed in a similar manner.

© 2016 Elsevier B.V. All rights reserved.

1. Introduction

Although it is simpler from an analytic perspective to characterize many of the processing flows important to industrial operations and experimental work as predominantly shearing or purely extensional in character, such a clear distinction is rarely achieved in practice. Indeed, the presence of walls in experimental devices inevitably leads to the introduction of shear at the boundaries, eliminating the possibility for such binary classifications and imparting instead a 'mixed' nature to the flow. An easily visualized example is that of flow through a hyperbolic microfluidic contraction channel, as studied in detail by Ober et al. [13]. Along the principal flow direction of such devices, the strain rate is theoretically constant and the nature of the flow purely elongational, permitting an estimate for the planar extensional viscosity to be obtained from measurements of the extra pressure drop and its elastic origins [13]. In the other two directions, however, shear from the confining walls cannot be ignored, and in practice this 'contaminates' the entire flow field. Indeed, in their studies of steady flow of Boger

fluids through arrays of cylinders, James et al. [7] concluded that their measurements of an enhanced pressure drop related to elastic effects was more attributable to normal stress differences arising from shear at the walls than those related to extension, thus highlighting the importance of considering the mixed nature of such flows during analysis.

For the case of polymer solutions in particular, imposed flows of pure shear or pure extension result in markedly different flow behavior and generate markedly different fluid stresses. In their pioneering work on flow classification, Tanner and Huilgol devised a system for characterizing flow strength based on the eigenvalues of the velocity gradient tensor of the flow field [18]. By this definition, if at least one of the eigenvalues of the flow field was positive and real, the flow was considered to be 'strong' [18,22]. Such flows, of which steady planar elongation is an example, are able to create significant distortions in the configuration of polymer chains above a certain critical elongation rate, resulting in coil-stretch transition and the growth of large viscoelastic fluid stresses. On the other hand, 'weak' flows, of which steady simple shear is an example, are incapable of significantly stretching the polymer chains [5]. One particular application of interest at the time for such a classification was the study of drag reduction in mixed flows of polymer solutions [17]. In his simulations, Tanner showed that a hysteresis

* Corresponding author.
E-mail addresses: cewagner@mit.edu (C.E. Wagner), gareth@mit.edu (G.H. McKinley).
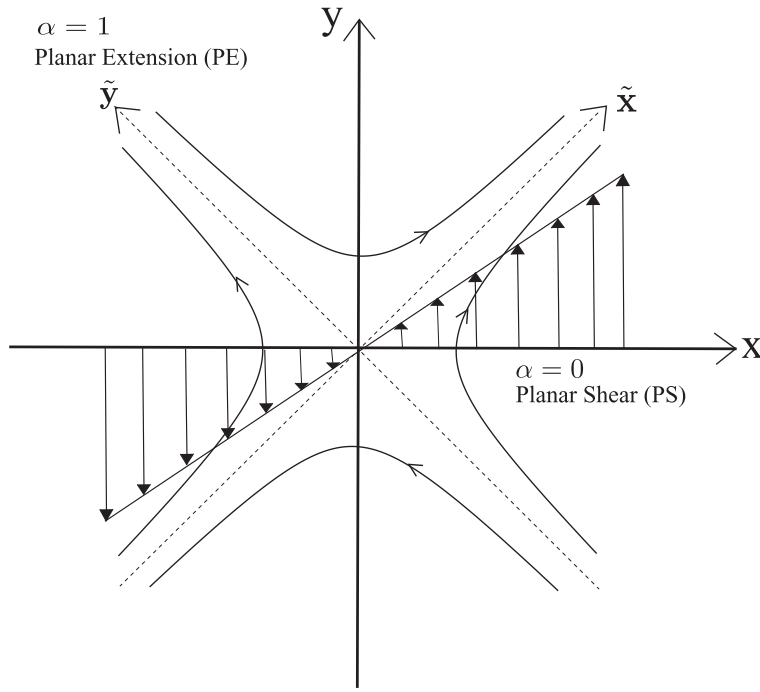
Fig. 1. Schematic depicting the kinematic decomposition of the planar mixed flows and the definition of the flow type parameter α in the non-rotated $\{\mathbf{x}, \mathbf{y}\}$ reference frame.

loop exists for the configuration of the polymer chains, which depends not only on the instantaneous strength of the flow, but also on the entire flow history [17]. Lagnado and Leal later investigated the effect of flow type on the stability of polymer solutions in the context of understanding polymer processing instabilities [10]. More recently, Thomases and Shelley have shown using numerical simulations of Oldroyd-B fluids that the magnitude of fluid stresses and the degree of mixing are highly dependent on flow strength (as measured by the Deborah number *De* which compares the time scale of the fluid to that of the flow, $De = \frac{\lambda_1}{T}$) in mixed flow devices [20,21]. By imposing a steady, spatially periodic background force on their simulated fluid, they determined the time-varying stress field arising from a velocity field generated by a four-roll mill geometry. Following the introduction of a small perturbation, they observed that for low Deborah numbers, the fluid response was slaved to the background forcing and no symmetry breaking was observed, while at higher flow strengths, asymmetries and instabilities dominated the flow patterns [21].

In this work, we begin with the approach of Fuller and Leal [5] and Hoffman and Shaqfeh [6] to demonstrate how mixed shear and extensional flows can be concisely characterized by a single flow-type parameter, denoted by α, and a deformation rate $|\dot{\gamma}|$. We consider two cases for such flows: firstly, constant deformation rate and an arbitrary (but constant) value of the flow-type parameter ($0 \leq \alpha \leq 1$), and then secondly a constant deformation rate with periodically varying flow-type parameter. This latter flow history can be envisioned to simulate flows through repeated expansions and contractions (see, for instance, the simulations of converging/ diverging microfluidic rectifiers studied by Sousa, et al. [16]) or through geometric arrays of cylinders [1]. We develop analytic expressions for the resulting stress fields of an Oldroyd-B fluid in such flow histories, and show that the coupling of the stress and velocity fields is strongly dependent on the relative flow and fluid time scales (as measured by the Deborah number $De = \frac{\lambda_1}{T}$), while the magnitude of the polymer stress response is primarily driven by the flow type parameter α and the Weissenberg number $Wi = \lambda_1|\dot{\gamma}|$. The latter two dimensionless parameters can be

combined into a single flow strength parameter $\lambda_1|\dot{\gamma}|\sqrt{\alpha} = Wi\sqrt{\alpha}$. Localized descriptions and decompositions of the state of the normal stress difference in a material element as being either an instantaneous 'viscoelastic shearing flow' or an instantaneous 'viscoelastic extensional flow' are thus not particularly helpful as the flow history of the material element is also important, unless $De \ll 1$. As a final example, we consider an approximate analysis of flow of an Oldroyd-B fluid close to a circular cylinder, and demonstrate using a decoupled kinematic analysis that the instantaneous polar angle θ of a material element serves as an exact allegory for the local flow type parameter α. We use this to calculate the evolution in the resulting stress field along a streamline, and demonstrate once again the coupled importance of the three dimensionless flow parameters *De, Wi,* and α.

2. Definition of the flow-type parameter

Following the method proposed by Fuller and Leal [5], the velocity gradient tensor for an arbitrary mixed planar flow can be expressed as

$$\nabla\mathbf{v} = \dot{\gamma}\begin{bmatrix} 0 & 1 & 0 \\ \alpha & 0 & 0 \\ 0 & 0 & 0 \end{bmatrix} \tag{1}$$

where $\mathbf{v}$ is the velocity vector, $\dot{\gamma}$ is the deformation rate, and α is the flow-type parameter. Clearly, when $\alpha = 0$, the flow is purely shear, with the velocity given by $\mathbf{v} = \dot{\gamma}\, x\, \hat{\mathbf{j}}$, while when $\alpha = 1$ the flow is purely elongational, as shown in Fig. 1. When $0 < \alpha < 1$, the flow is mixed, with both shear and elongation contributing to its nature. This formulation is the mathematical analog to the experimental four-roll mill device invented by Taylor [19], and recently refined on a microfluidic scale by Lee et al. [12] in a geometry which permits the kinematics of a flow to be continuously varied by modifying the relative strengths of two opposing cross-flows.

In order to characterize the flow strength according to the framework developed by Tanner and Huilgol [18], it is necessary to

determine the eigenvalues and eigenvectors of the velocity gradient tensor. Following Hoffman and Shaqfeh [6] who characterized velocity fields similarly in their Brownian Dynamics simulations of the hysteretic behavior of polymer chains in mixed flows, we wish to rotate the Cartesian coordinate axis associated with elongation in order for it to align with the vector defining the direction of principal elongation for any arbitrary mixed flow. As such, when $\alpha = 0$, the direction of shearing occurs along $\hat{\mathbf{j}}$ as defined in Fig. 1. We proceed by rotating the original axes {$\mathbf{x}$, $\mathbf{y}$} in Fig. 1 in order to align the base vector $\hat{\mathbf{i}}$ with the direction of primary stretching: the eigenvector associated with the positive real eigenvalue of the velocity gradient tensor for an arbitrary flow type $0 \leq \alpha \leq 1$. Following standard procedures, the eigenvalues are found to be

$$\beta_1 = \sqrt{\alpha}\dot{\gamma}, \quad \beta_2 = -\sqrt{\alpha}\dot{\gamma}, \quad \beta_3 = 0$$

and the corresponding eigenvectors are

$$\mathbf{X}_1 = \begin{bmatrix} 1 \\ \sqrt{\alpha} \\ 0 \end{bmatrix}, \ \mathbf{X}_2 = \begin{bmatrix} 1 \\ -\sqrt{\alpha} \\ 0 \end{bmatrix}, \ \mathbf{X}_3 = \begin{bmatrix} 0 \\ 0 \\ 1 \end{bmatrix}.$$

The angle around $\hat{\mathbf{k}}$ through which $\hat{\mathbf{i}}$ must be rotated in order to align with $\mathbf{X}_1$ can easily be found to be $\theta = \cos^{-1}(\frac{1}{\sqrt{1+\alpha}})$, from which it follows that the rotation matrix $\mathbf{R}$ is given by

$$\mathbf{R} = \frac{1}{\sqrt{1+\alpha}}\begin{bmatrix} 1 & \sqrt{\alpha} & 0 \\ -\sqrt{\alpha} & 1 & 0 \\ 0 & 0 & 1 \end{bmatrix}. \tag{2}$$

Note that for steady simple shearing flows ($\alpha = 0$), the velocity gradient tensor is nilpotent and hence the eigenvalues are all identically zero. As such, there is no direction of principal elongation and no rotation occurs ($\theta = \cos^{-1}(1) = 0$). The maximum rotation angle occurs for planar elongational flow ($\alpha = 1$), with a rotation angle of $\theta = \cos^{-1}(\frac{1}{\sqrt{2}}) = \frac{\pi}{4}$ radians. The rotated axes {$\tilde{\mathbf{x}}$, $\tilde{\mathbf{y}}$} are also sketched in Fig. 1. The velocity gradient tensor in this rotated frame is then

$$\tilde{\nabla}\ \tilde{\mathbf{v}} = \mathbf{R} \cdot \nabla\ \mathbf{v} \cdot \mathbf{R}^T = \dot{\gamma}\sqrt{\alpha}\begin{bmatrix} 1 & \frac{1-\alpha}{\sqrt{\alpha}} & 0 \\ 0 & -1 & 0 \\ 0 & 0 & 0 \end{bmatrix} \tag{3}$$

where in this rotated frame, the meaning of the flow-type parameter α is all the more clear, with only terms on the main diagonal retained in pure elongation ($\alpha = 1$), and only off-diagonal terms retained in steady simple shear ($\alpha = 0$).

It is worth noting that it is certainly possible for α to assume a negative value, i.e. $-1 \leq \alpha < 0$. When $\alpha = -1$, the velocity field corresponds to pure solid body rotation, and a fluid element in the flow follows a circular trajectory, while when $-1 < \alpha < 0$, the velocity field is a combination of shearing and solid body rotation, and the same element follows an elliptical trajectory [5]. However, when the eigenvalues for this flow are calculated using the procedure detailed above, one obtains a zero eigenvalue and a conjugate pair of imaginary ones:

$$\beta_1 = i\sqrt{\alpha}\dot{\gamma}, \quad \beta_2 = -i\sqrt{\alpha}\dot{\gamma}, \quad \beta_3 = 0.$$

Applying the flow characterization procedure of Tanner and Huilgol [18], this flow is determined to be exclusively weak, and critical values of polymer chain stretch will therefore never be achieved. Furthermore, the components of the velocity gradient tensor associated with extension will be imaginary for all time, since solid body rotation does not contribute to deviatoric fluid stresses. Therefore, although negative values of the flow type parameter α can certainly define physically realizable flow fields, in the sections to follow we analyze flows for $0 \leq \alpha \leq 1$ exclusively as a result of our interest in studying mixed shear and elongational flows.

3. The Oldroyd-B stress field for steady, planar mixed flows

The Oldroyd-B constitutive model assumes a solution of infinitely extensible Hookean dumbbells with constant viscosity $\eta_0 = \eta_s + \eta_p$, where η_s and η_p denote the solvent and polymer contributions to the viscosity, respectively. The relaxation time of the dumbbells is given by λ_1, and the retardation time λ_2 is defined as $\lambda_2 = \frac{\eta_s}{\eta_s + \eta_p}\lambda_1 = \frac{\eta_s}{\eta_0}\lambda_1$, leading to the complete constitutive equation as given in [2]

$$\boldsymbol{\tau} + \lambda_1\boldsymbol{\tau}_{(1)} = -\eta_0\left(\boldsymbol{\gamma}_{(1)} + \lambda_2\boldsymbol{\gamma}_{(2)}\right) \tag{4}$$

where $\boldsymbol{\gamma}_{(1)}$ is the rate of strain tensor given by

$$\boldsymbol{\gamma}_{(1)} = \left\{(\nabla\ \mathbf{v}) + (\nabla\ \mathbf{v})^T\right\} \tag{5}$$

and the subscript $()_{(1)}$ denotes the upper convected derivative

$$()_{(1)} = \frac{\partial()}{\partial t} + \mathbf{v} \cdot \nabla() - \left\{(\nabla\ \mathbf{v})^T \cdot () + () \cdot (\nabla\ \mathbf{v})\right\}. \tag{6}$$

We consider first the case of steady mixed planar flow, where the strain rate $\dot{\gamma}$ and the flow-type parameter α are uniform throughout the flow field and constant in time. Since this flow is homogeneous, it is convenient to break the stress tensor in the rotated frame into two parts: a solvent contribution

$$\boldsymbol{\tau}_s = -\eta_s\boldsymbol{\gamma}_{(1)}, \tag{7}$$

and a polymer contribution $\boldsymbol{\tau}_p$, where from Eq. (4) it follows that the governing equation for the polymer contribution is of Upper Convected Maxwell form

$$\boldsymbol{\tau}_p + \lambda_1\boldsymbol{\tau}_{p(1)} = -\eta_p\boldsymbol{\gamma}_{(1)}. \tag{8}$$

It is clear then that our analysis can be applied to either Upper Convected Maxwell or Oldroyd-B fluids. In the latter case, the appropriate contribution from the Newtonian solvent (which has no memory of previous deformations and responds instantaneously to the flow strength and type) can simply be reintroduced to the obtained stress field as an algebraic addition. Furthermore, we note that in resolving the Oldroyd-B stress field from the unperturbed Newtonian velocity profile, we are using a second-order retarded-motion expansion, which is valid for the low Deborah number flows principally considered in this study [2] and allows us to make progress analytically. In general, however, at larger *De*, the velocity, pressure and stress fields are coupled, and a complete numerical solution of the momentum and constitutive equations would be required for quantitative results.

Solving for the various components of Eq. (8) and expressing them in component form in the rotated coordinate frame, we obtain a coupled set of differential equations for the fluid stresses:

$$\lambda_1\frac{d\tilde{\tau}_{xx,p}}{dt} = -(1 - 2Wi\sqrt{\alpha})\tilde{\tau}_{xx,p} - 2\eta_p\dot{\gamma}\sqrt{\alpha} \tag{9}$$
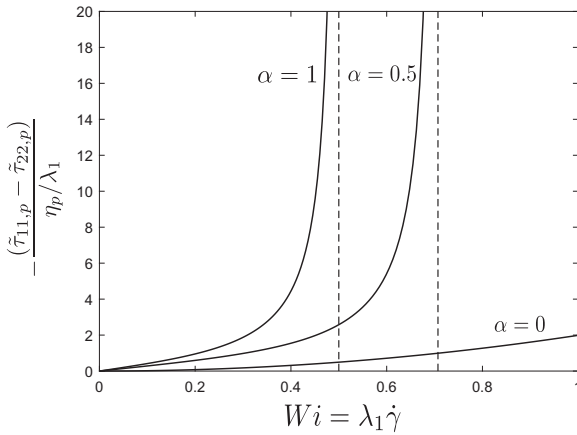
$$\lambda_1\frac{d\tilde{\tau}_{xy,p}}{dt} = -\tilde{\tau}_{xy,p} + Wi(1-\alpha)\tilde{\tau}_{xx,p} - \eta_p\dot{\gamma}(1-\alpha) \tag{10}$$

$$\lambda_1\frac{d\tilde{\tau}_{yy,p}}{dt} = -(1 + 2Wi\sqrt{\alpha})\tilde{\tau}_{yy,p} + 2Wi(1-\alpha)\tilde{\tau}_{xy,p} + 2\eta_p\dot{\gamma}\sqrt{\alpha} \tag{11}$$

$$\lambda_1\frac{d\tilde{\tau}_{zz,p}}{dt} = -\tilde{\tau}_{zz,p} \tag{12}$$

Eqs. (9)–(12) can be solved analytically, in combination with an initial condition of zero initial polymer stress ($\tilde{\boldsymbol{\tau}}_p(t=0) = 0$), to yield time varying expressions for the various fluid stresses:

$$\tilde{\tau}_{xx,p}(t) = -\frac{2\dot{\gamma}\sqrt{\alpha}\eta_p}{1 - 2Wi\sqrt{\alpha}}\left[1 - \exp\left(-(1 - 2Wi\sqrt{\alpha})t/\lambda_1\right)\right] \tag{13}$$

Fig. 2. Normalized steady-state first normal stress difference as a function of the Weissenberg number for various values of the flow-type parameter α in the rotated reference frame. The dashed lines indicate the critical value of Wi at which the flows with extensional components diverge: i.e. when the flow strength approaches $\dot{\gamma}\lambda_1\sqrt{\alpha} = 1/2$.

$$\tilde{\tau}_{xy,p}(t) = -\frac{\dot{\gamma}\eta_p(1-\alpha)}{1-2Wi\sqrt{\alpha}}\left[1 - \exp\left(-(1-2Wi\sqrt{\alpha})t/\lambda_1\right)\right] \quad (14)$$

$$\tilde{\tau}_{yy,p}(t) = \frac{\dot{\gamma}\eta_p(1-\alpha)^2}{2\sqrt{\alpha}(1-2Wi\sqrt{\alpha})}\left[\exp\left(-(1-2Wi\sqrt{\alpha})t/\lambda_1\right)\right.$$
$$\left. - \exp\left(-(1+2Wi\sqrt{\alpha})t/\lambda_1\right)\right]$$
$$+ \frac{2\dot{\gamma}\eta_p(\sqrt{\alpha} - Wi(1+\alpha^2))}{(1-4Wi^2\alpha)}$$
$$\times\left[1 - \exp\left(-(1+2Wi\sqrt{\alpha})t/\lambda_1\right)\right] \quad (15)$$

$$\tilde{\tau}_{zz,p}(t) = 0 \quad (16)$$

The total stresses are found by adding the appropriate contribution of the solvent stress tensor $\tilde{\boldsymbol{\tau}}_s = -\eta_s\tilde{\boldsymbol{\gamma}}_{(1)}$ to Eqs. (13)–(16). At steady state, we obtain the well-known results that, for steady simple shear ($\alpha = 0$):

$$\lim_{t/\lambda_1\to\infty}\left(\tilde{\tau}_{xx} - \tilde{\tau}_{yy}\right) \to 2\eta_0\dot{\gamma}^2(\lambda_1 - \lambda_2) \quad (17)$$

$$\lim_{t/\lambda_1\to\infty}\tilde{\tau}_{xy} \to -\eta_0\dot{\gamma} \quad (18)$$

and in planar elongation ($\alpha = 1$)

$$\lim_{t/\lambda_1\to\infty}\left(\tilde{\tau}_{xx} - \tilde{\tau}_{yy}\right) \to -4\eta_0\dot{\gamma}\frac{\left(1 - 4\lambda_2/\lambda_1 Wi^2\right)}{\left(1 - 4Wi^2\right)} \quad (19)$$

$$\lim_{t/\lambda_1\to\infty}\tilde{\tau}_{xy} \to 0. \quad (20)$$

In Fig. 2, the steady-state values of the first polymer normal stress difference $N_1 = -(\tilde{\tau}_{11,p} - \tilde{\tau}_{22,p})$ in the rotated reference frame, normalized by the effective modulus $G = \eta_p/\lambda_1$, are plotted as functions of the Weissenberg number $Wi = \lambda_1\dot{\gamma}$ for various values of the flow type parameter α.

As is seen in Fig. 2, when the flow is in steady simple shear, the first polymer normal stress difference normalized by the effective modulus is proportional to Wi^2 over the entire range of deformation rates simulated, as this 'weak' flow never reaches the coil-stretch transition, and hence the polymer stresses are always bounded. As extensional character is added to the flow, and $\alpha \to 1$, this normalized stress difference is initially finite, and in fact linearly proportional to Wi when the flow strength is well below $\dot{\gamma}\lambda_1\sqrt{\alpha} = 1/2$, but diverges for all $\alpha \neq 0$ very sharply as this limit

is reached. These conclusions can be seen succinctly by examining the steady state value of N_1/G for general α in the limit of small Weissenberg number. Retaining only terms up to second order in Wi, we obtain

$$-\frac{\left(\tilde{\tau}_{xx,p} - \tilde{\tau}_{yy,p}\right)}{\eta_p/\lambda_1} \to 4Wi\sqrt{\alpha} - 2\left(1 - \alpha^2\right)Wi^2. \quad (21)$$

In steady simple shear ($\alpha = 0$), only the second term proportional to Wi^2 remains, as expected. Conversely, when $\alpha \neq 0$, the first order term in Wi dominates at small values of the flow strength, and the normalized first normal stress difference is linearly proportional to the Weissenberg number Wi. The change in sign results from the definition of the direction of shear in Fig. 1 as $\hat{\mathbf{j}}$ in the original non-rotated frame or $\tilde{\mathbf{y}}$ in the rotated one. Based on this convention, when $\alpha = 0$,

$$-(\tilde{\tau}_{11,p} - \tilde{\tau}_{22,p}) = -(\tilde{\tau}_{yy,p} - \tilde{\tau}_{xx,p}),$$

while when the flow has an extensional component and non-zero eigenvalues exist, $\tilde{\mathbf{x}}$ is defined as the direction of principal elongation, and hence

$$-(\tilde{\tau}_{11,p} - \tilde{\tau}_{22,p}) = -(\tilde{\tau}_{xx,p} - \tilde{\tau}_{yy,p}).$$

With this behavior established, it is of interest to examine the fluid stress response in a more complex case when the flow-type parameter is not fixed, and the flow is not necessarily given sufficient residence time to reach steady state.

4. Planar flows with time-varying flow type parameter α

We consider now the slightly more complex case of a flow with constant deformation rate $\dot{\gamma}$ but periodically varying flow-type parameter α. Physically, this type of flow field is reminiscent of flow through a repeated array of hyperbolic expansions and contractions, or flow through a simplified geometric array of cylinders or other objects. We designate the oscillation period for the flow type as T, and thus the oscillation frequency is given by $\omega = \frac{2\pi}{T}$ and the time varying expression for the flow-type parameter is taken to be

$$\alpha(t) = \frac{1}{2}(1 \pm \cos(\omega t)).$$

By fixing the Weissenberg number at $Wi = \lambda_1\dot{\gamma} = 0.1$ so that no singular behavior is observed in the stress field, and varying the kinematic sequencing (whether the flow was initialized in shear or extension) and the relative time scales of the oscillation and fluid response, we can observe the importance of the flow history on the resulting stresses.

The governing equations for the polymer stresses (Eqs. (9)–(12)) derived in the previous section still hold, although an additional equation must be added to account for the time variation of the flow-type parameter α. The sign of the time derivative of α is positive when the flow is initiated as a sine wave in steady simple shear ($\alpha = 0$), and negative in the opposite case when the flow is initiated in pure elongation ($\alpha = 1$), and hence the input function is a cosine wave

$$\frac{d\alpha}{dt} = \pm\frac{1}{2}\omega\sin(\omega t). \quad (22)$$

Eqs. (9)–(12) in combination with Eq. (22) are then solved numerically using the stiff Matlab ODE solver ode15s with the initial condition of zero polymer stress at $t = 0$. In Fig. 3, we plot the evolution of the normal and shear stresses as well as the flow-type parameter α over one oscillation period in the rotated coordinate frame. We consider both the cases where the flow is initialized in shear (Fig. 3a and c) as well as in extension (Fig. 3b and d), and also consider two values for the oscillation period. In the first instance, the oscillation period T is taken to be significantly longer

$$\alpha(\tau) = \frac{1}{2}\left(1 - \cos(2\pi\tau)\right)$$

$$\alpha(\tau) = \frac{1}{2}\left(1 + \cos(2\pi\tau)\right)$$
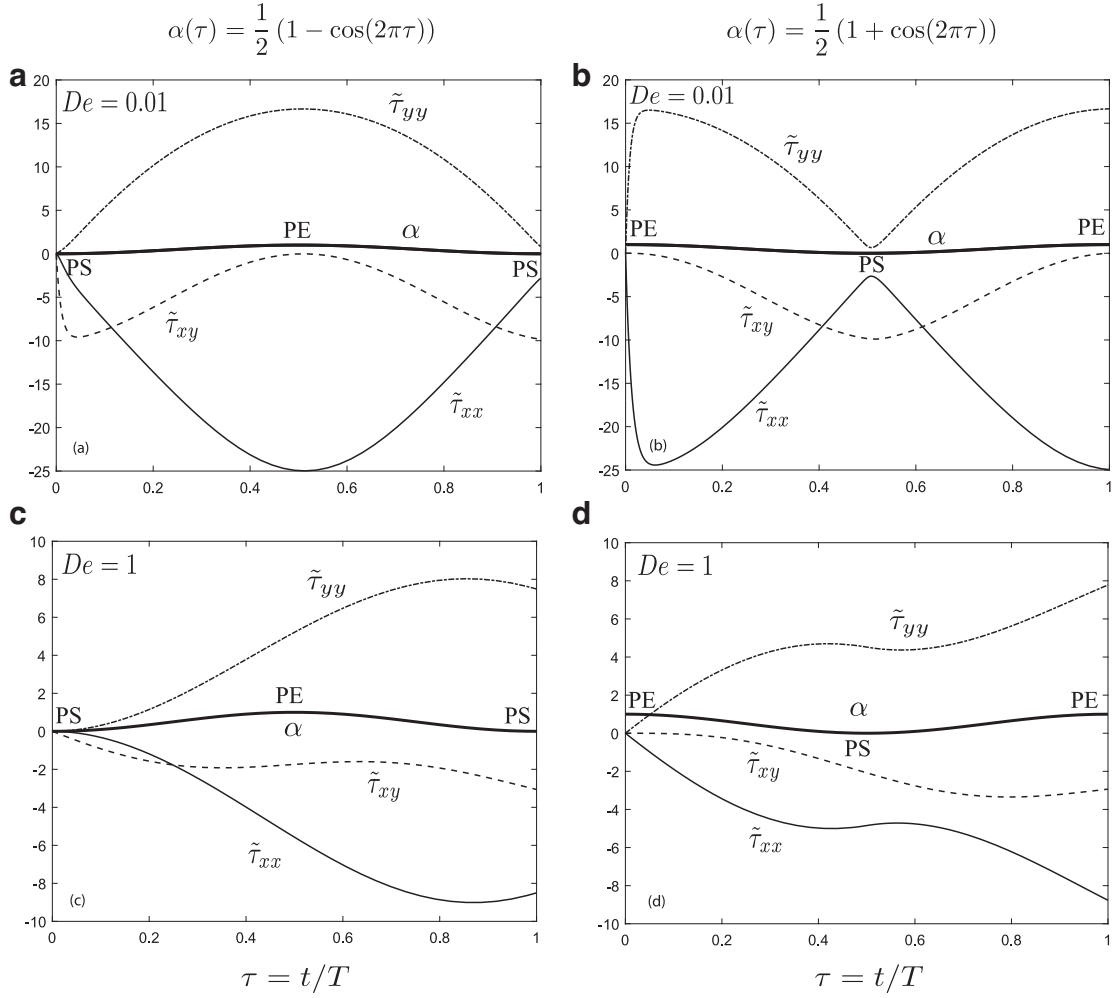
Fig. 3. Evolution of shear and normal stresses for flows with periodically varying flow-type parameter α for different Deborah numbers and kinematic sequencing (shear or extensional flow initialization) in the rotated coordinate frame. PE denotes pure elongation, while PS denotes pure shear.

than the fluid relaxation time such that $De = \lambda_1/T = 0.01$ (Fig. 3a and b), and in the second instance the oscillation period is taken to be identical to the fluid relaxation time, yielding an effective Deborah number of $De = 1$ (Fig. 3c and d).

Clearly, the Deborah number has a large effect on the stress profile. In low Deborah number flows (Fig. 3a and b), the stress field is synchronized with the velocity field exactly, and the shear and normal stresses reach their steady-state maxima when the flow is purely shear (Eqs. (17) and (18)) or purely extensional (Eqs. (19) and (20)). It should be noted that the apparent lack of symmetry for the case when the flow is initialized in extension (Fig. 3b) is a result of the stresses being initialized at zero. In subsequent periods, the flow is indeed symmetric about $\tau = t/T = 0.5$. Conversely, when the oscillation period and fluid relaxation time are comparable, the stress and velocity fields no longer align (Fig. 3c and d). In this situation, whether the flow is initialized in shear or extension becomes significant, as can be seen in the starkly different evolution of the fluid stresses over the course of one oscillation cycle. Furthermore, although the stresses do equilibrate to a time periodic steady state (or "alternating") value that depends on the flow-type parameter α after a number of oscillation periods, the steady state stress values expected for either steady simple shear and pure elongation at low De (c.f. Eqs. (17)–(20)) are never attained.

This effect of oscillation time scale can also be demonstrated nicely by analyzing the rate of energy dissipated per unit volume by the flow over time,

$$\phi = -\tilde{\boldsymbol{\sigma}} : \tilde{\nabla}\,\tilde{\mathbf{v}} = -(-p\mathbf{I} + \tilde{\boldsymbol{\tau}}) : \tilde{\nabla}\,\tilde{\mathbf{v}} \tag{23}$$

where p is the pressure field and $\mathbf{I}$ is the identity matrix. The isotropic pressure field does not dissipate power in an incompressible fluid, and hence Eq. (23) reduces to

$$\phi = -\tilde{\boldsymbol{\tau}} : \tilde{\nabla}\,\tilde{\mathbf{v}}. \tag{24}$$

Taking this inner product yields an expression for the rate of dissipated energy

$$\phi_{tot}(t) = -\dot{\gamma}\sqrt{\alpha}\left(\tilde{\tau}_{xx} + \frac{1-\alpha}{\sqrt{\alpha}}\tilde{\tau}_{xy} - \tilde{\tau}_{yy}\right) \tag{25}$$

where the expressions for $\tilde{\tau}_{xx}$, $\tilde{\tau}_{xy}$, and $\tilde{\tau}_{yy}$ are found from the solutions of Eqs. (19) and (20). This result can be separated into two components, the first from dissipation related to shear stresses:
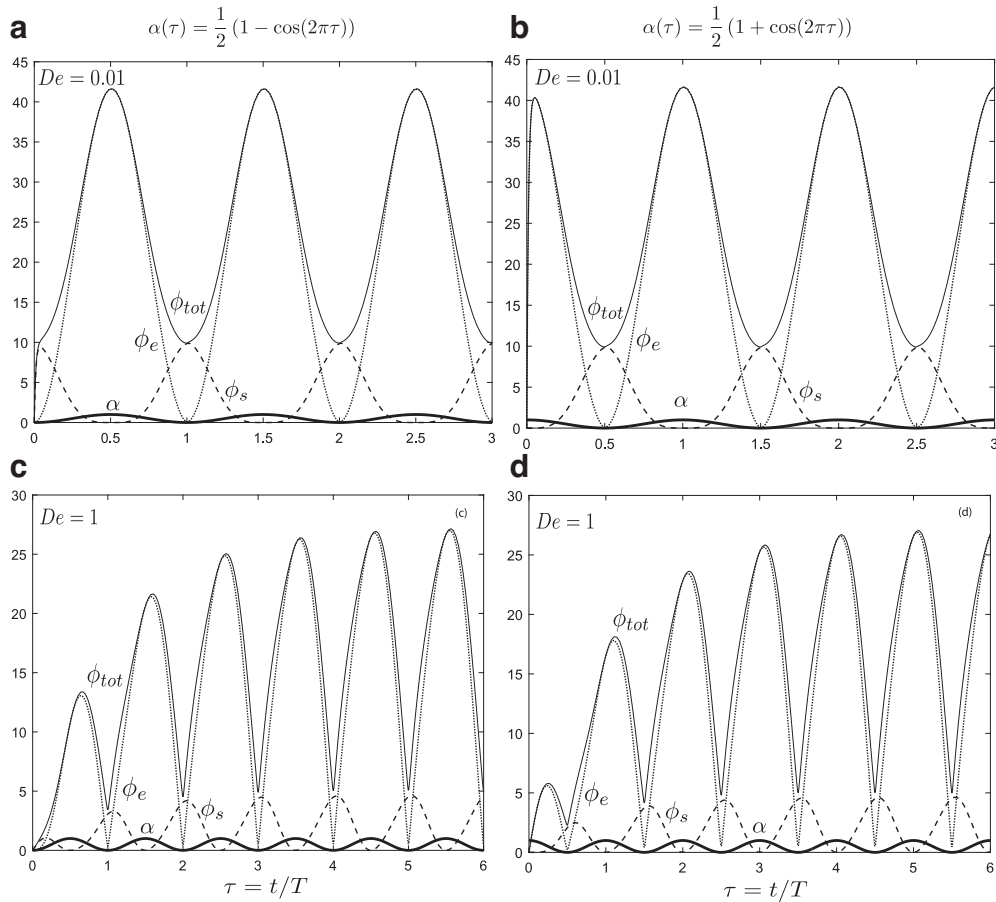
$$\phi_s(t) = -\dot{\gamma}\sqrt{\alpha}\left(\frac{1-\alpha}{\sqrt{\alpha}}\tilde{\tau}_{xy}\right) = -(1-\alpha)\dot{\gamma}\,\tilde{\tau}_{xy} \tag{26}$$

and the other from dissipation related to the extensional normal stress difference:

$$\phi_e(t) = -\dot{\gamma}\sqrt{\alpha}(\tilde{\tau}_{xx} - \tilde{\tau}_{yy}). \tag{27}$$

It is clear from these expressions that in steady simple shear ($\alpha = 0$), the dissipation in the system comes entirely from the shear stress (i.e. the normal stresses are purely elastic in character),

Fig. 4. Rate of energy dissipation $\phi_{tot} = \phi_e$ (solid line) $+\phi_s$ (dashed line) for flows with periodically varying flow-type parameter α for different Deborah numbers and different initialization conditions (shear or extension).

whereas in planar elongation ($\alpha = 1$), there are no shear stresses and the normal stress difference is completely dissipative in character.

In Fig. 4, the total rate of dissipated energy as well as the individual contributions from the shear and extensional terms and the flow-type parameter α are plotted for the same conditions as in Fig. 3, but over several oscillation cycles.

As expected, at low Deborah numbers (Fig. 4a and b), the shear and extensional contributions to the rate of dissipated energy align exactly with the flow type from the onset of the flow, with the total dissipated power maximized in the strong pure extensional flow (when $\alpha \sim O(1)$) and minimized in the weak steady simple shear flow. Conversely, in higher *De* number cases (Fig. 4c and d), there is an initial phase lag between the maximal power dissipation and the flow-type parameter, and several oscillations are required before a steady alternating state is achieved. It is interesting to note, in keeping with the result obtained previously for the stresses, that even at this higher Deborah number alternating steady state, the power dissipated is lower than in the case where the oscillation period far exceeds the fluid relaxation time (*De* ∼ $O(0.01)$). This can be understood by the fact that the fluid is becoming increasingly elastic. The residence time of the chains in the region of strong elastic stretching is correspondingly shorter at high *De*; even though the velocity field is nominally purely elongational over the course of an oscillation, the phase lag never quite allows the rate of dissipation to reach steady state and energy is stored elastically in the flow.

As a final example, we apply these concepts developed in steady and time periodic flows to help understand the more com-

plex case of flow past a circular cylinder, where fluid elements transition between predominantly shearing and predominantly extensional kinematics while traveling along a streamline that passes close to the cylinder surface.

5. Flow past a circular cylinder

We analyze the stresses that develop in a material element of an Oldroyd-B fluid flowing along two different streamlines close to the surface of a circular cylinder, as shown in Fig. 5. Although the non-Newtonian nature of the fluid in reality would alter the calculated velocity field, for the sake of simplicity, we impose the velocity field for a Newtonian fluid and calculate the resulting stresses that develop from the non-Newtonian constitutive equation, as done by Chilcott and Rallison in their study of creeping flows of polymer solutions past cylinders and spheres [3].

As a result of the presence and geometry of the obstacle, the nature of the flow evolves between extension-dominated and shear-dominated over the course of the trajectory, with rotation also being important when viscosity is considered [9]. Physically, as we are interested in studying the simple case of laminar, symmetric streamlines and unseparated flow, we must consider a system with *Re* ≪ 1 [9]. It is well known, however, that in the regime of viscous creeping flow, there is no solution to the Navier–Stokes equations that can satisfy both no-slip on the cylinder boundary and finite velocity and pressure at infinity where the flow is uniform; this is Stokes' Paradox [9]. Oseen provided an explanation for this paradox with his observation that the assumption of negligible inertia (*Re* ≪ 1) cannot hold both close to the cylinder, where the
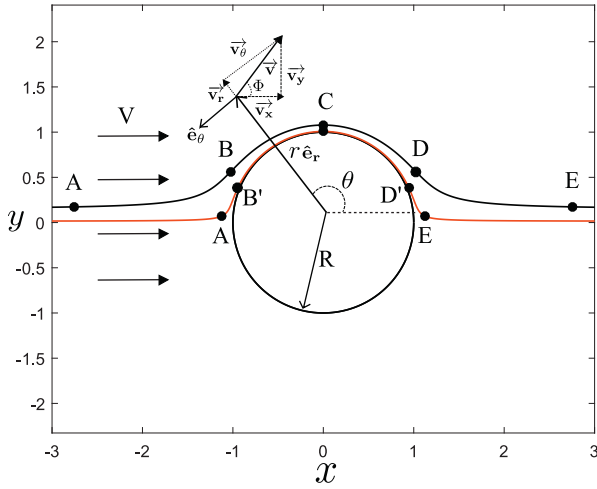
Fig. 5. Diagram depicting two different streamlines and the parameters considered for flow past a circular cylinder. The flow is initialized outside the domain shown at radial position of $r_0 = 5R$ (where R is the radius of the cylinder), and an angle of $\theta_0 = \frac{99\pi}{100}$ for the black curve and $\theta_0 = \frac{999\pi}{1000}$ for the red curve. Point A is at $\theta = \frac{49\pi}{50}$, point C is at $\theta = \frac{\pi}{2}$ ($r_c = 1.08R$ for the black curve and $r_c = 1.01R$ for the red curve), and Point E is at $\theta = \frac{\pi}{50}$. As explained in the section to follow, Points B and D correspond to the value of θ for which the flow strength parameter $Wi\sqrt{\alpha}$ is maximized, which differs for the two curves. (For interpretation of the references to color in this figure legend, the reader is referred to the web version of this article.)

Reynolds number is defined based on the diameter of the cylinder, and at infinity, where the more appropriate length scale is the radial distance from the center of the cylinder [14]. He proposed a composite solution to this problem, whereby the velocity field is assumed to be composed of a primary component and a perturbation component, with the inertial terms of the Navier–Stokes equations retained for these perturbed quantities [11]. By matching this solution with one valid closer to the cylinder, an approximate piecewise solution can be obtained (an excellent discussion is provided by Lamb [11]). Faxén also proposed a resolution to this paradox by considering flow past a circular cylinder confined between two parallel plates in order to limit the size of the domain of interest [4]. In a similar effort, Chilcott and Rallison considered two simplified versions of the problem: flow past a cylindrical bubble, where the boundary condition at the cylinder edge is modified to that of zero tangential stress, and flow past a solid cylinder with the external domain confined to an annulus containing the cylindrical obstacle [3].

Proudman and Pearson [15] provide a uniformly valid approximate solution for the stream function:

$$\psi_{PP} = -\frac{VR\sin\theta}{2\log Re}\left(\frac{R}{r} - \frac{r}{R} + \frac{2r}{R}\log\left(\frac{r}{R + Re\, r}\right)\right) \tag{28}$$

from which the radial and tangential velocities, respectively, are found to be

$$v_{r,PP} = \frac{1}{r}\frac{\partial\psi}{\partial\theta} = -\frac{VR\cos\theta}{2\log Re}\left(\frac{R}{r^2} - \frac{1}{R} + \frac{2}{R}\log\left(\frac{r}{R + Re\, r}\right)\right) \tag{29}$$

and

$$v_{\theta,PP} = -\frac{\partial\psi}{\partial r} = \frac{VR\sin\theta}{2\log Re}\left(-\frac{R}{r^2} - \frac{1}{R} + \frac{2}{R}\log\left(\frac{r}{R + Re\, r}\right) + \frac{2}{R + Re\, r}\right), \tag{30}$$

where V is the velocity of the unperturbed fluid stream, R is the radius of the cylinder, and the directions of r and θ are as shown in Fig. 5. The Reynolds number is that based on the cylinder diameter: $Re = 2VR/\nu$, where $\nu = \eta_0/\rho$ is the kinematic viscosity of the fluid. Clearly, these velocities are not well defined infinitely far from the cylinder due to the logarithmic terms, but the approximation is valid and accurate close to the cylinder surface.

Despite the existence of these matched asymptotic expressions, the aim of our present study is to analyze in a simple fashion the role of the velocity gradient tensor, and illustrate how changes in the kinematic character of the flow affect the resulting stress fields. As such, we wish to consider instead the simplest possible stream function for flow past a circular cylinder, which of course is that for potential flow, the equations of which are given by [9]

$$\psi_{potential} = V\sin\theta\left(r - \frac{R^2}{r}\right), \tag{31}$$

$$v_{r,potential} = \frac{1}{r}\frac{\partial\psi}{\partial\theta} = V\cos\theta\left(1 - \frac{R^2}{r^2}\right) \tag{32}$$

and

$$v_{\theta,potential} = -\frac{\partial\psi}{\partial r} = -V\sin\theta\left(1 + \frac{R^2}{r^2}\right) \tag{33}$$

The difficulty arises from the fact that the potential flow field is only valid in the limit of negligible viscous effects, while experiments show that for real fluids, symmetric and unseparated streamlines are only achieved at low Reynolds numbers, where viscosity dominates [9].

While it is clear, at the very least from the presence of terms involving logarithms of the Reynolds number in the perturbation solution of Proudman and Pearson, that these solutions are fundamentally different, it is interesting to note that if we consider their viscous solution in the limit of very low Reynolds numbers ($Re \ll 1$), and very closer to the cylinder surface, such that $r = R(1 + \epsilon)$, where ϵ is a positive quantity satisfying $\epsilon \ll 1$, some common features arise. Ignoring the magnitude of the velocity vectors, we can instead consider the *shape* of the streamlines very close to the cylinder by calculating the instantaneous polar angle of the velocity vector along the trajectory, denoted by ϕ in Fig. 5. Geometrically, ϕ is defined as

$$\phi(\theta) = \arctan\left(\frac{v_y(\theta)}{v_x(\theta)}\right) = \arctan\left(\frac{v_r\sin\theta + v_\theta\cos\theta}{v_r\cos\theta - v_\theta\sin\theta}\right). \tag{34}$$

It is straightforward to show that both the potential flow solution and the Proudman and Pearson viscous solution, in the limit of $Re \ll 1$ and $r \to R$, reduce to

$$\phi(\theta) \to \arctan\left(\frac{-2\sin\theta\cos\theta}{1 - \cos 2\theta}\right). \tag{35}$$

Although this result does not indicate that the velocity fields converge (indeed, since the Proudman and Pearson solution satisfies no slip at the cylinder surface while potential flow does not, it is clear that the magnitudes of the velocity fields will not be the same), it does show that the streamline shapes are, in fact, identical at low Reynolds numbers and close to the cylinder surface.

Using the definition of the velocity gradient tensor in cylindrical coordinates, we obtain, for the potential flow case

$$\nabla\mathbf{v} = \begin{bmatrix} \dfrac{\partial v_r}{\partial r} & \dfrac{\partial v_\theta}{\partial r} & 0 \\ \dfrac{1}{r}\dfrac{\partial v_r}{\partial\theta} - \dfrac{v_\theta}{r} & \dfrac{1}{r}\dfrac{\partial v_\theta}{\partial\theta} + \dfrac{v_r}{r} & 0 \\ 0 & 0 & 0 \end{bmatrix}$$

$$= \frac{2VR^2}{r^3}\begin{bmatrix} \cos\theta & \sin\theta & 0 \\ \sin\theta & -\cos\theta & 0 \\ 0 & 0 & 0 \end{bmatrix} \tag{36}$$

for which the associated eigenvalues are

$$\beta_1 = \frac{2VR^2}{r^3}, \quad \beta_2 = -\frac{2VR^2}{r^3}, \quad \beta_3 = 0.$$

It is clear then that for this problem, the appropriate measure of the flow strength in the direction of primary elongation is $\frac{V}{R}\left(\frac{R}{r}\right)^3$,

from which it follows that a suitable Weissenberg number to compare the local strength of the flow along a streamline with the relaxation time of the fluid is

$$Wi = \frac{\lambda_1 V}{R} \xi^{-3} \qquad (37)$$

where ξ is the radial position normalized by the radius of the cylinder, $\xi = \frac{r}{R}$. In order to simply compare the characteristic flow and fluid time scales, we can define the Deborah number for this flow as

$$De = \frac{\lambda_1 V}{R}. \qquad (38)$$

Since we consider points in the flow field where $r \approx R$, these two non-dimensional parameters coincide quite closely; what changes for the material element as it flows around the cylinder is the flow *type*.

In contrast to the spatially uniform, homogeneous velocity gradient tensor obtained for the case of planar mixed flow, the velocity gradient for potential flow past a cylinder depends on the spatial position within the flow. As a result, the direction of primary stretch also varies throughout the flow field, and so it is not possible to rotate the global cylindrical coordinate axes to coincide for all times with specific eigenvectors. We show instead that the local value of the circumferential angle θ effectively characterizes this flow in the same way that the flow-type parameter α did for the planar mixed flow discussed previously.

Specifically, the shear rate and rate of angular rotation for the irrotational potential flow velocity field are given by

$$\dot{\gamma}_{pot} = \frac{\partial v_\theta}{\partial r} - \frac{v_\theta}{r} + \frac{1}{r} \frac{\partial v_r}{\partial \theta} = \frac{4VR^2}{r^3} \sin\theta \qquad (39)$$

and

$$\omega_{pot} = -\frac{\partial v_\theta}{\partial r} - \frac{v_\theta}{r} + \frac{1}{r} \frac{\partial v_r}{\partial \theta} = 0, \qquad (40)$$

while analysis of Eq. (3) reveals that the equivalent results for the arbitrary mixed planar flow considered earlier (based on which the flow-type parameter α is defined) are

$$\dot{\gamma}_{xy,mf} = \dot{\gamma}(1 - \alpha) \qquad (41)$$

and

$$\omega_{mf} = -\dot{\gamma}(1 - \alpha). \qquad (42)$$

Comparison of Eqs. (39) and (41) demonstrates that for potential flow, the magnitude of the local velocity gradient is given by $\frac{4VR^2}{r^3}$ and the flow-type parameter is

$$\alpha = 1 - \sin\theta. \qquad (43)$$

A simple analysis of Eq. (36) reveals that at the leading and trailing poles of the cylinder ($\theta \to 0, \pi$), the velocity gradient tensor is given by

$$\nabla \mathbf{v} = \frac{2VR^2}{r^3} \begin{bmatrix} \pm1 & 0 & 0 \\ 0 & \mp1 & 0 \\ 0 & 0 & 0 \end{bmatrix} \qquad (44)$$

indicating that the flow is purely extensional, with stretching in the tangential direction $\hat{e}_\theta$ and compression in the radial direction $\hat{e}_r$ along the upstream stagnation plane ($\theta = \pi$) and stretching in the radial direction and compression in the tangential direction along the downstream stagnation plane ($\theta = 0$) based on the configuration described in Fig. 5. Conversely, at the equator $\theta = \frac{\pi}{2}$, the velocity gradient tensor is given by

$$\nabla \mathbf{v} = \frac{2VR^2}{r^3} \begin{bmatrix} 0 & 1 & 0 \\ 1 & 0 & 0 \\ 0 & 0 & 0 \end{bmatrix} \qquad (45)$$

indicating that the flow at this position is in pure shear. At all other circumferential angles along the trajectory, the flow is mixed, with both shearing and extensional components. However, the flow is vorticity free everywhere.

It is straightforward to verify that the velocity gradient tensor for the Proudman and Pearson stream function is given by

$$\nabla \mathbf{v}_{PP} = \frac{VR}{r \log Re}$$
$$\times \begin{bmatrix} \cos\theta\left(\dfrac{R}{r^2} - \dfrac{1}{R + Re\ r}\right) & \sin\theta\left(\dfrac{R}{r^2} + \dfrac{R}{(R + Re\ r)^2}\right) & 0 \\ \sin\theta\left(\dfrac{R}{r^2} - \dfrac{1}{R + Re\ r}\right) & -\cos\theta\left(\dfrac{R}{r^2} - \dfrac{1}{R + Re\ r}\right) & 0 \\ 0 & 0 & 0 \end{bmatrix}. \qquad (46)$$

At the poles of the cylinder ($\theta = 0, \pi$), the flow is again purely extensional, as in the case of potential flow. However, since the velocity gradient tensor is no longer symmetric, it is clear that one of the effects of including viscosity in the stream function is to introduce vorticity to the flow.

The expressions for the shear rate and the rate of angular rotation in cylindrical coordinates corresponding to the Proudman and Pearson solution can be found to be:

$$\dot{\gamma}_{PP} = \frac{\partial v_\theta}{\partial r} - \frac{v_\theta}{r} + \frac{1}{r} \frac{\partial v_r}{\partial \theta} = \frac{VR\sin\theta}{r \log Re}\left(\frac{2R}{r^2} - \frac{Re\ r}{(R + Re\ r)^2}\right) \qquad (47)$$

and

$$\omega_{PP} = -\frac{\partial v_\theta}{\partial r} - \frac{v_\theta}{r} + \frac{1}{r} \frac{\partial v_r}{\partial \theta} = \frac{-VR\sin\theta}{r \log Re}\left(\frac{2R + Re\ r}{(R + Re\ r)^2}\right). \qquad (48)$$

Analysis of Eq. (46) reveals that at the equator ($\theta = \frac{\pi}{2}$), the Proudman and Pearson flow is in a combination of pure shear and solid body rotation, as opposed to pure shear alone for potential flows. However, if we consider the limit of $Re \ll 1$ and $r = R(1 + \epsilon)$ (for which it was found previously that the shape of the streamlines for the potential and Proudman and Pearson flows converge), it is clear that Eqs. (47) and (48) take on the limiting forms of

$$\lim_{Re \to 0} \dot{\gamma}_{PP} = \frac{2V}{R \log Re} \sin\theta \qquad (49)$$

and

$$\lim_{Re \to 0} \omega_{PP} = -\frac{2V}{R \log Re} \sin\theta. \qquad (50)$$

Comparison of Eqs. (49) and (50) with their arbitrary mixed planar flow analogs (Eqs. (41) and (42)) reveals that in this limit, as for potential flow, $\alpha = 1 - \sin\theta$ is also the appropriate measure of the flow-type parameter for the Proudman and Pearson solution.

In what proceeds, as a result of the convergence of the streamline shape and flow-type parameter α in this limit for both flows (as well as the fact that the introduction of solid body rotation through vorticity in the Proudman and Pearson solution does not give rise to any additional fluid stresses due to the frame invariance of the convected derivatives used to construct the constitutive equations), we analyze the stress fields using the simpler potential flow velocity field given in Eqs. (31)–(33). Indeed, the use of this potential flow solution is consistent with the condition of zero tangential stress at the cylinder surface, which is the "cylindrical bubble" case considered by Chilcott and Rallison [3]. Additional discussions regarding the advantages and approximations inherent in considering 'viscous potential flows' are discussed in the book by Joseph [8].

Using the velocity gradient tensor for the potential flow field (Eq. (36)) and the Oldroyd-B constitutive equation (Eq. (8)), we can proceed to develop the governing differential equations for the evolution in the fluid polymer stresses. The procedure is identical to that followed for planar mixed flow, with the exception that the
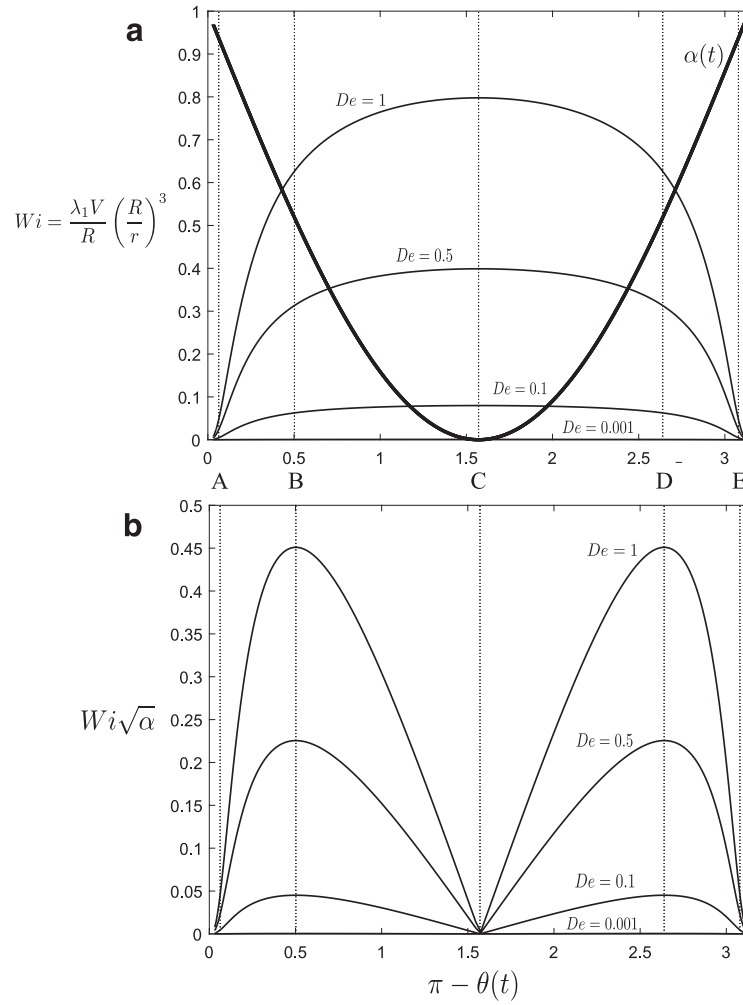
Fig. 6. (a) Weissenberg number plotted as a function of circumferential angle $\theta(t)$ for four values of the Deborah number ($De = 0.001$, $De = 0.1$, $De = 0.5$, and $De = 1$) for the black streamline from Fig. 5 (initialized at $\theta_0 = \frac{99\pi}{100}$). The flow-type parameter is also plotted, where $\alpha(t) = 1 - \sin\theta(t)$. (b) Flow strength parameter $Wi\sqrt{\alpha}$ plotted as a function of circumferential angle $\theta(t)$ for the same four values of the Deborah number considered in (a).

velocity gradient tensor for this flow is no longer spatially homogeneous. As a result, the advective term in the material derivative is not identically zero. Once again, to obtain the total stresses, the appropriate solvent stress term is added (see Eq. (7)). Note also that the tilde superscript is not used, as the reference frame is no longer rotating but aligned with the global $\{r, \theta\}$ system. Combining all of the terms in Eq. (8) we obtain:

$$(rr): 3\lambda_1 \frac{d\tau_{rr,p}}{dt} = -\tau_{rr,p} + \frac{2v_\theta \lambda_1}{r}\tau_{r\theta,p} + \frac{4VR^2}{r^3}$$
$$\times \left(\lambda_1(\tau_{rr,p}\cos\theta + \tau_{r\theta,p}\sin\theta) - \eta_p\cos\theta\right) \quad (51)$$

$$(r\theta): 3\lambda_1 \frac{d\tau_{r\theta,p}}{dt} = -\tau_{r\theta,p} - \frac{\lambda_1 v_\theta}{r}(\tau_{rr,p} - \tau_{\theta\theta,p})$$
$$+ \frac{2VR^2}{r^3}\sin\theta\left(\lambda_1(\tau_{rr,p} + \tau_{\theta\theta,p}) - 2\eta_p\right) \quad (52)$$

$$(\theta\theta): 3\lambda_1 \frac{d\tau_{\theta\theta,p}}{dt} = -\tau_{\theta\theta,p} - \frac{2v_\theta \lambda_1}{r}\tau_{r\theta,p} + \frac{4VR^2}{r^3}$$
$$\times \left(\lambda_1(\tau_{r\theta,p}\sin\theta - \tau_{\theta\theta,p}\cos\theta) + \eta_p\cos\theta\right) \quad (53)$$

$$(zz): \lambda_1 \frac{d\tau_{zz,p}}{dt} = -\tau_{zz,p} \quad (54)$$

$$\frac{dr}{dt} = V\cos\theta\left(1 - \frac{R^2}{r^2}\right) \quad (55)$$

$$\frac{d\theta}{dt} = -\frac{V}{r}\sin\theta\left(1 + \frac{R^2}{r^2}\right) \quad (56)$$

where v_r and v_θ are the radial and tangential velocity components for the potential flow fields, respectively, given in Eqs. (32) and (33). Once again, these equations are solved numerically using the stiff Matlab ODE solver ode15s and the initial condition of zero stress at $t = 0$, with the position initialized to r_0 and θ_0, such that the resulting streamline followed passes close to the surface of the cylinder, but is not the stagnation streamline. Following this initialization, the streamline coordinates $(r_s(t), \theta_s(t))$ throughout the trajectory of the material element are found by integrating Eqs. (55) and (56) in time. The resulting calculated streamlines for two different flow initialization points are shown by the red and black curves in Fig. 5. The corresponding values of the Lagrangian velocity and position are then used to integrate Eqs. (51)–(53) and find the evolution in the stresses.

We begin by considering the kinematics of the flow. Since potential flow is imposed in both cases, we consider only the evolution in the local value of $Wi(r, \theta_s)$ based on the black streamline from Fig. 5 (initialized at $\theta_0 = \frac{99\pi}{100}$) for now. In Fig. 6a, the Weissenberg number (Eq. (37)) is plotted as a function of the circumferential angle for flows with four different Deborah numbers
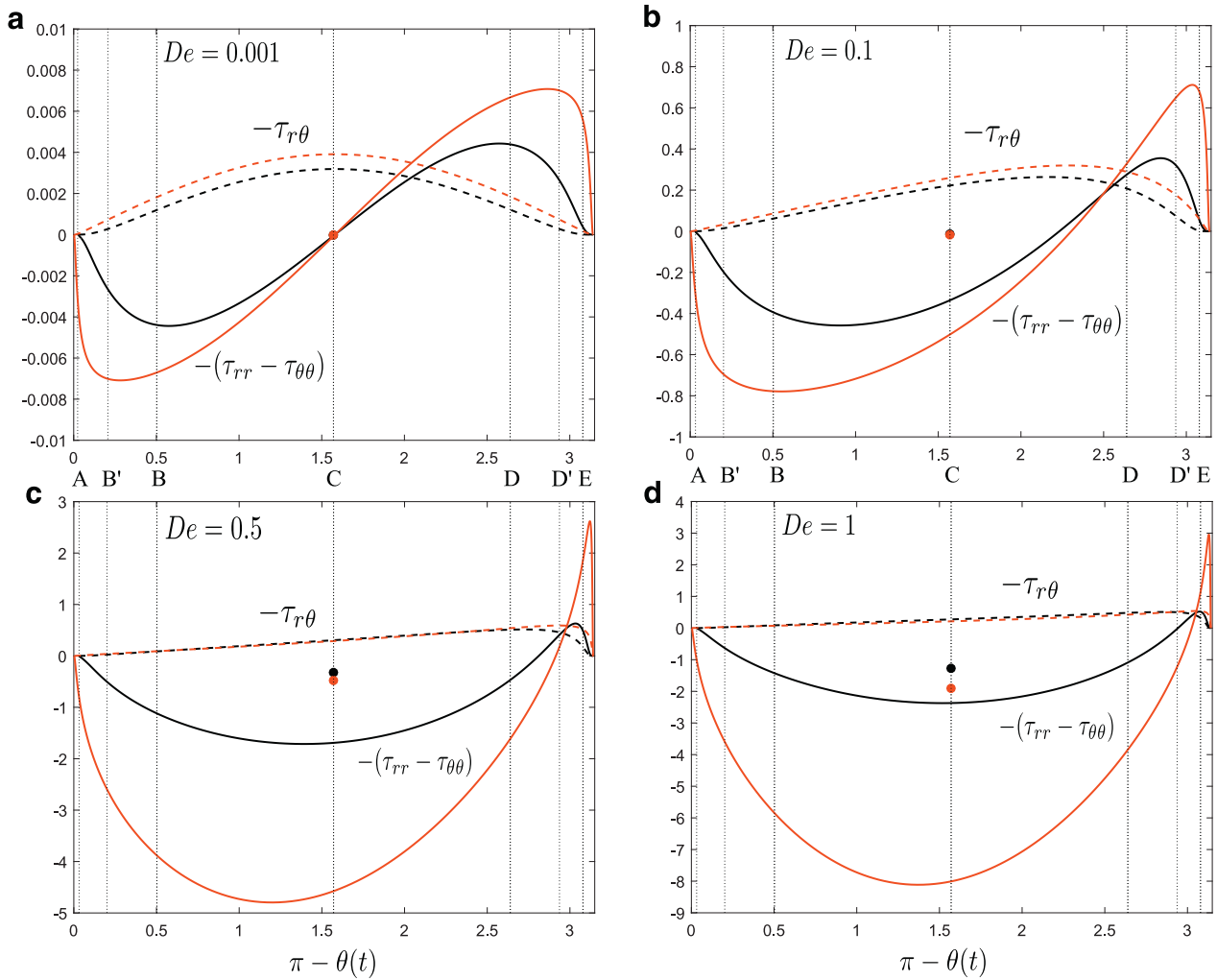
Fig. 7. First normal stress difference and shear stress for viscous potential flow of an Oldroyd-B fluid past a circular cylinder for (a) $De = 0.001$, (b) $De = 0.1$, (c) $De = 0.5$, and (d) $De = 1$. The black and red curves correspond to the black and red streamlines from Fig. 5, where $\theta_0 = \frac{99\pi}{100}$ for the black streamline and $\theta_0 = \frac{999\pi}{1000}$ for the red streamline. The solid dots correspond to the steady-state value of the normal stress difference (Eqs. (13) and (15)) for a shear flow with the same value of Wi as that achieved at the equator (Point C, $\theta = \frac{\pi}{2}$), where the flow is nominally purely shearing. (For interpretation of the references to color in this figure legend, the reader is referred to the web version of this article.)

($De = 0.001$, $De = 0.1$, $De = 0.5$, and $De = 1$). The flow-type parameter $\alpha(t)$ as given in Eq. (43) is also shown. In Fig. 6b, the total flow strength parameter $Wi\sqrt{\alpha}$ (the product of the two parameters considered in Fig. 6a) is plotted as a function of circumferential angle for the same four values of the Deborah number. The points A, B, C, D, and E correspond to those labeled in Fig. 5.

Beginning with Fig. 6a, we see that fore-aft symmetry is maintained at all values of De considered as a result of the imposed potential velocity field. For the entire path around the cylinder, the value of the Weissenberg number is bounded by $0 < Wi < De$, and indeed from Fig. 6 we see that Wi and De coincide most closely when the material element is close to the cylinder surface (near the equator, Point C, where $\theta = \frac{\pi}{2}$). The behavior of the flow strength parameter, plotted in Fig. 6b, is noticeably different, but still fore-aft symmetric for all values of De considered. The flow strength drops to zero far from the cylinder (Points A and E), as a result of $Wi \to 0$ at these positions due to its inverse cubic dependence on radial position (Eq. (37)). The flow strength parameter is also zero at the equator (Point C, $\theta = \frac{\pi}{2}$), where the flow is nominally purely shearing and hence the flow-type parameter is $\alpha = 0$. Points B and D (and analogously Points B′ and D′ for the red streamline in Fig. 5 initialized at $\theta_0 = \frac{999\pi}{1000}$) are therefore defined as the values of the circumferential angle θ where the flow

strength parameter is maximized. This maximization can be readily performed by expressing the flow-type parameter α and the radial position r in terms of θ through Eq. (43) and the combination of Eqs. (55) and (56), respectively. In the latter case, we obtain

$$r(\theta) = \frac{C}{2\sin\theta} + R\sqrt{1 + \frac{C^2}{4R^2\sin\theta}},$$

where C is a constant related to the Lagrangian position at which the streamline was initialized

$$C = \sin\theta_0\left(r_0 - \frac{R^2}{r_0}\right).$$

In Fig. 7, the first normal stress difference, $N_1 = -(\tau_{rr} - \tau_{\theta\theta})$, and the shear stress $(-\tau_{r\theta})$ normalized by the effective modulus $G = \eta_0/\lambda_1$ are plotted against the circumferential angle $\theta(t)$, for a fluid element initialized on both the red and black streamlines from Fig. 5 for the same four values of the Deborah number considered in Fig. 6.

For the lowest Deborah number case considered ($De = 0.001$), both the shear stress and the first normal stress difference are larger for the streamline that passes closer to the surface of the cylinder (the red one). The shear stress is fore-aft symmetric (in keeping with the kinematics shown in Fig. 6), always positive, and
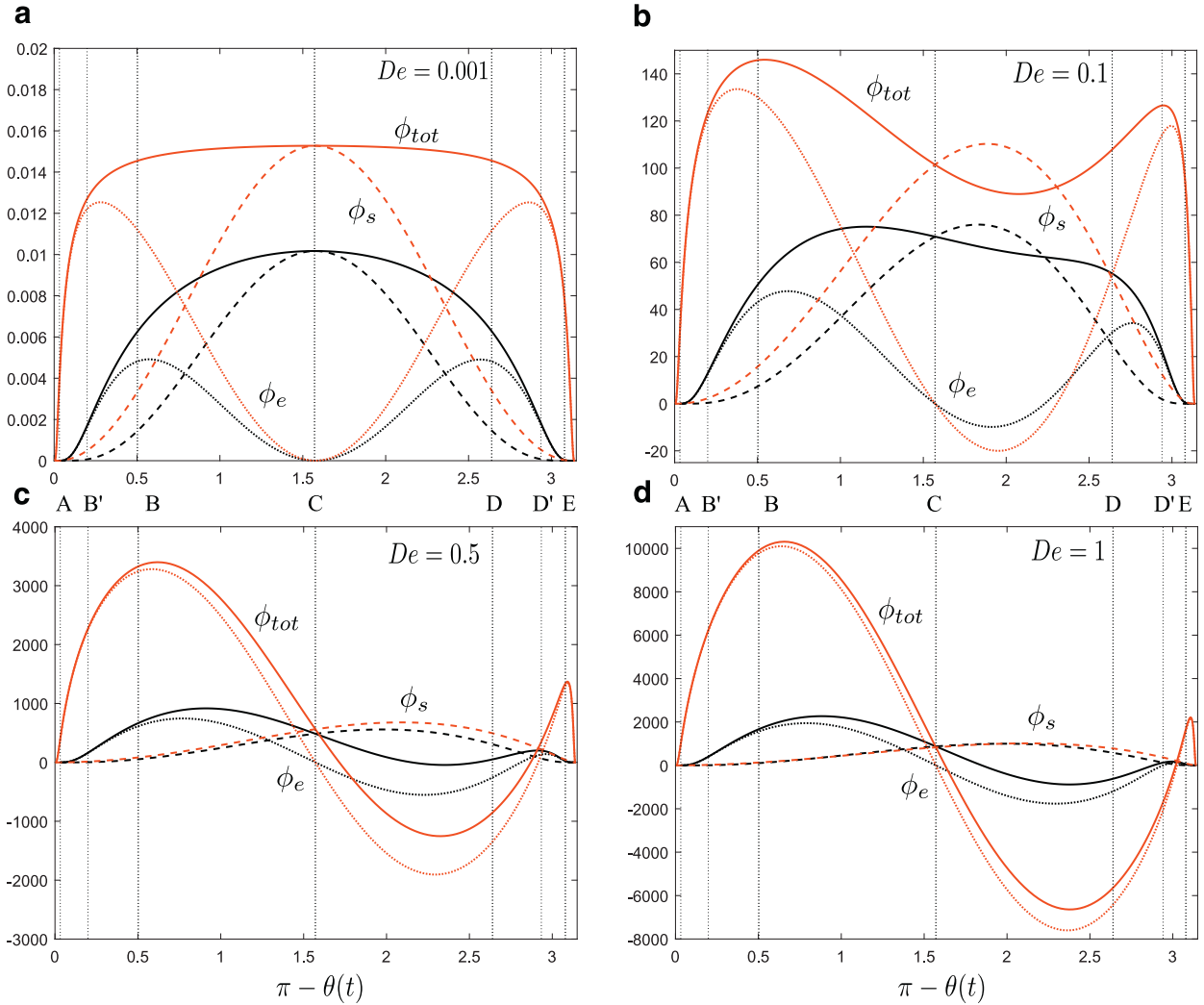
Fig. 8. Total rate of dissipated energy ϕ_{tot} for viscous potential flow of an Oldroyd-B fluid element flowing past a circular cylinder and the individual contributions coming from shear (ϕ_s) and elongation (ϕ_e) for (a) $De = 0.001$, (b) $De = 0.1$, (c) $De = 0.5$, and (d) $De = 1$. The black and red curves correspond to the black and red streamlines from Fig. 5, where $\theta_0 = \frac{99\pi}{100}$ for the black streamline and $\theta_0 = \frac{999\pi}{1000}$ for the red streamline. (For interpretation of the references to color in this figure legend, the reader is referred to the web version of this article.)

maximized at $\theta = \frac{\pi}{2}$ where the velocity field is in pure shear (Eq. (45)). In contrast, N_1 is antisymmetric; it is positive for $0 < \theta(t) < \frac{\pi}{2}$, indicating a tensile stress, and negative, or compressive, for $\frac{\pi}{2} < \theta(t) < \pi$, with both the compressive and tensile stress differences being maximized at Points B and D, respectively, where the flow strength parameter $Wi\sqrt{\alpha}$ is at its maximum. As the Deborah number increases ($De \rightarrow 1$), the stresses lose their symmetry and hence their synchronicity with the kinematics. Consistent with the simulations of Chilcott and Rallison [3], the stresses are larger on the upstream side of the cylinder than the downstream side, and since the polymer chains can now be increasingly deformed by these relatively stronger flows, the magnitudes of the normal stresses begin to exceed that of the shear stress. Additionally, it is clear that the stresses begin to take on an asymptotic limiting profile corresponding to a linear variation in the shear stress from zero upstream (Point A, $\theta \rightarrow \pi$) until very close to the downstream wake (Point E, $\theta \rightarrow 0$). Similarly, the normal stress differences converge to a nearly parabolic profile except for a narrow region near $\theta \rightarrow 0$ where a sharp local peak in the normal stress difference develops. This corresponds to the elastic stress boundary layer in the wake discussed by Chilcott and Rallison [3]. The invariant asymptotic shape of these profiles for $De \geq 1$ suggests

that a solution based on matched asymptotic expansions for an inner flow (near $\theta \sim 0$) and an outer flow ($\pi > \theta > 0$) may be useful in the future.

We can also compare the normal stress difference computed at Point C ($\theta = \frac{\pi}{2}$), where the flow is nominally purely shearing, with that expected from a steady simple shear flow at a shear rate of $Wi = \lambda_1\dot{\gamma}_c = De(R/r_c)^3$ and $\alpha = 0$ using our analytic solutions from Eqs. (13)–(15). These predictions are shown by the filled circles at each Point C in Fig. 7 for both streamlines considered. Clearly, this steady state result is only a good prediction for the normal stress difference in the limit of very small Deborah numbers ($De = 0.001$ in Fig. 7a) i.e. where the flow is slowly varying. In this limit, the polymer chains are able to respond sufficiently quickly to changes in the local flow type $\alpha(r, \theta)$ such that the local stress fields align with the flow kinematics, and have essentially forgotten about their prior deformation history. In contrast, as the flow strength increases ($De \rightarrow 1$), the result from steady simple shear flow begins to dramatically under-predict that observed when the entire flow history is considered. In this regime, the large stretches that the polymer chains incurred near the poles of the cylinder (when the flow is extensional in character) are not forgotten by the time the equator is reached, and indeed this effect

becomes more pronounced for the red streamline which passes closer to the surface of the cylinder where chain stretch is even more significant.

In a similar way to our analysis for the periodically varying flow-type parameter discussed in Section 4, we can analyze the local rate of dissipated energy and its origins for a material element as it flows around the cylinder. In Fig. 8, we plot the individual and total contributions to the dissipated power per unit volume

$$\phi_{tot} = \phi_e + \phi_s = -\boldsymbol{\tau} : \nabla \mathbf{v} = -\frac{2VR^2}{r^3}(\cos\theta(\tau_{rr} - \tau_{\theta\theta}) + 2\sin\theta\,\tau_{r\theta})$$

$$(57)$$

as a function of angular position for both the red and black streamlines and the same values of the Deborah number considered in Fig. 7.

For all Deborah numbers considered, the power dissipated by viscoelastic normal stress differences and in shear by a material element on a streamline that passes closer to the surface of the cylinder (the red streamline from Fig. 5) exceeds that of the more distant streamline, in keeping with the stress results from Fig. 7. Once again, the power dissipation in the low Deborah number case ($De = 0.001$) is fore-aft symmetric, reaching a maximum entirely from shear contributions at $\theta = \frac{\pi}{2}$. Further, in keeping with the stress results in Fig. 7, the rate of energy dissipated by the normal stress difference in extension is lower than that due to shear, and is maximized very near Points B and D for the black curve ($\theta_0 = \frac{99\pi}{100}$) and B′ and D′ for the red curve ($\theta_0 = \frac{999\pi}{1000}$), where the flow strength parameter $Wi\sqrt{\alpha}$ is maximized. As the flow strength is incremented and the polymer chains become increasingly stretched ($De \rightarrow 1$), this symmetry is lost, and power dissipated by the viscoelastic extensional stress difference begins to exceed that due to shear. Since the shear stress is purely dissipative, the rate of energy dissipation from shear remains positive for the entire material element trajectory at all De considered, but is maximized increasingly far downstream, analogously to the result for shear stresses (Fig. 7). In contrast, the elastic normal stress difference can store energy or dissipate it depending on the flow type and the sign of the stress. At higher De, the kinematics and stresses lose their synchronicity due to the advective terms in the equations. At the equator ($\theta = \frac{\pi}{2}$), the locally dissipated energy results totally from the shearing. However, the large first normal stress differences are advected into the wake and remain compressive even in the downstream half of the flow. Correspondingly, the local rate of energy dissipation here is negative, indicating energy storage, in this portion of the flow field. All together, these dramatic changes in the shape and symmetry of the local stress fields and power dissipation further highlight the importance of understanding both the instantaneous local flow character and the entire flow history in viscoelastic fluid flow analysis.

6. Conclusion

To conclude, we have demonstrated using the technique outlined in [5,6,18] that the character of planar mixed flows can be quantified fully by a flow-type parameter α, which varies between $\alpha = 0$ in pure shear and $\alpha = 1$ in pure extension and a flow strength parameter $\lambda_1\dot{\gamma}\sqrt{\alpha}$. We have developed analytic expressions for the time dependent normal and shear stresses arising in an Oldroyd-B fluid undergoing steady, homogeneous planar mixed flow. Building on these results, we next considered the case of a periodically varying flow-type parameter (reminiscent of flows through repeated hyperbolic expansions/contractions or through geometric arrays of submerged obstacles). The resulting stress fields in the cases of 'fast' and 'slow' flows (as compared to the relaxation time of the fluid) revealed that flow strength and

history are critically important in terms of predicting stresses. Indeed, when the Deborah number becomes large ($De \sim O(1)$), the stresses never achieve the steady state values that were derived in the first part of the paper in either shear or extension, resulting in lower dissipated power and a loss of synchronicity with the velocity field. Furthermore, whether the flow is initialized in shear or extension has a large effect on the stress fields over a single oscillation cycle. Finally, we considered the more complex problem of the flow of an Oldroyd-B fluid past a cylindrical bubble. We justified the use of the potential velocity field for understanding the basic structural evolution of the flow stresses, and showed that for this spatially inhomogeneous flow, the local polar angle θ is analogous to the flow type parameter α developed for homogeneous planar mixed flows. This allowed us to understand the evolution in the kinematics of fluid elements on two different streamlines as they flow close to the cylindrical bubble. In the limit of vanishingly small De, the stress fields and kinematics are synchronized, and the normal stress difference obtained at the equator ($\theta = \frac{\pi}{2}$), where the flow is nominally purely shearing, matches exactly with that which would have been predicted for a steady simple shear flow. At $De \sim O(1)$, however, the steady simple shear flow result for the normal stress difference is no longer a good prediction for the value of N_1 at the equator. In fact, the values of the first normal stress difference at the equator (where $\alpha = 0$) and in the wake (where $\alpha \sim O(1)$) are comparable in magnitude but have very different origins and contributions to the rate of dissipated energy in the flow. In this way, it is clear that local flow type can only be an indicator of the expected stress fields in the limit of slow and slowly-varying flows ($De \ll 1$); for all other cases, the polymer chains have a vivid memory of their stretching history, and this must be accounted for when interpreting the local measures of the state of stress in a strongly viscoelastic liquid.

References

[1] F.J. Alcocer, P. Singh, Permeability of periodic arrays of cylinders for viscoelastic flows, Phys. Fluids 14 (7) (2002) 2578–2581, doi:10.1063/1.1483301.

[2] R.B. Bird, R.C. Armstrong, O. Hassager, Dynamics of Polymeric Liquids, Fluid Mechanics, vol. 1, Wiley and Sons, 1987.

[3] M.D. Chilcott, J.M. Rallison, Creeping flow of dilute polymer solutions past cylinders and spheres, J. Non-Newton. Fluid Mech. 29 (1988) 381–432.

[4] H. Faxén, The resistance against the movement of a rigid sphere in viscous fluids, which is embedded between two parallel layered barriers, Ann. Phys. 68 (1922) 89–119.

[5] G.G. Fuller, L.G. Leal, The effects of conformation-dependent friction and internal viscosity on the dynamics of the nonlinear dumbbell model for a dilute polymer solution, J. Non-Newton. Fluid Mech. 8 (3--4) (1981) 271–310, doi:10.1016/0377-0257(81)80026-2.

[6] B.D. Hoffman, E.S.G. Shaqfeh, The dynamics of the coil-stretch transition for long, flexible polymers in planar mixed flows, J. Rheol. 51 (5) (2007) 947, doi:10.1122/1.2754293.

[7] D.F. James, R. Yip, I.G. Currie, Slow flow of Boger fluids through model fibrous porous media, J. Rheol. 56 (5) (2012) 1249, doi:10.1122/1.4732533.

[8] D.D. Joseph, T. Funada, J. Wang, Potential Flows of Viscous and Viscoelastic Fluids, Cambridge University Press, New York, 2008.

[9] P.K. Kundu, I.M. Cohen, D.R. Dowling, Fluid Mechanics, fifth ed., Elsevier Academic Press, 2012.

[10] R.R. Lagnado, L.G. Leal, The stability of two-dimensional linear flows of an Oldroyd-type fluid, J. Non-Newton. Fluid Mech. 18 (1985) 25–59.

[11] H. Lamb, Hydrodynamics, fourth ed., Cambridge University Press, Cambridge, UK, 1916.

[12] J.S. Lee, R. Dylla-Spears, N.P. Teclemariam, S.J. Muller, Microfluidic four-roll mill for all flow types, Appl. Phys. Lett. 90 (7) (2007) 2005–2008, doi:10.1063/1.2472528.

[13] T.J. Ober, S.J. Haward, C.J. Pipe, J. Soulages, G.H. McKinley, Microfluidic extensional rheometry using a hyperbolic contraction geometry, Rheol. Acta 52 (6) (2013) 529–546, doi:10.1007/s00397-013-0701-y.

[14] C. Oseen, Neuere Methoden und Ergebnisse in der Hydrodynamik, Akademische Verlagsgesellschaft, Leipzig, 1927.

[15] I. Proudman, J.R.A. Pearson, Expansions at small Reynolds numbers for the flow past a sphere and a circular cylinder, J. Fluid Mech. 2 (03) (1957) 237, doi:10.1017/S0022112057000105.

[16] P.C. Sousa, F.T. Pinho, M.S.N. Oliveira, M.A. Alves, Efficient microfluidic rectifiers for viscoelastic fluid flow, J. Non-Newton. Fluid Mech. 165 (11-12) (2010) 652–671, doi:10.1016/j.jnnfm.2010.03.005.

[17] R.I. Tanner, Stresses in dilute solutions of bead-nonlinear-spring macromolecules. III. Friction coefficient varying with dumbbell extension, Trans. Soc. Rheol. 19 (1975) 557–582.

[18] R.I. Tanner, R.R. Huilgol, On a classification scheme for flow fields, Rheol. Acta 14 (11) (1975) 959–962.

[19] G.I. Taylor, The formation of emulsions in definable fields of flow, Proc. R. Soc. Lond. A 146 (1934) 501–523.

[20] B. Thomases, M. Shelley, Emergence of singular structures in Oldroyd-B fluids, Phys. Fluids 19 (10) (2007) 1–12, doi:10.1063/1.2783426.

[21] B. Thomases, M. Shelley, J.L. Thiffeault, A Stokesian viscoelastic flow: transition to oscillations and mixing, Physica D 240 (20) (2011) 1602–1614, doi:10.1016/j.physd.2011.06.011.

[22] R.L. Thompson, P.R. Souza Mendes, Considerations on kinematic flow classification criteria, J. Non-Newton. Fluid Mech. 128 (2-3) (2005) 109–115, doi:10.1016/j.jnnfm.2005.04.002.